

DiffTex: Differentiable Texturing for Architectural Proxy Models

WEIDAN XIONG, CSSE, Shenzhen University, China
 YONGLI WU, CSSE, Shenzhen University, China
 BOCHUAN ZENG, CSSE, Shenzhen University, China
 JIANWEI GUO, Beijing Normal University, China
 DANI LISCHINSKI, The Hebrew University of Jerusalem, Israel
 DANIEL COHEN-OR, CSSE, Shenzhen University, China
 HUI HUANG*, CSSE, Shenzhen University, China

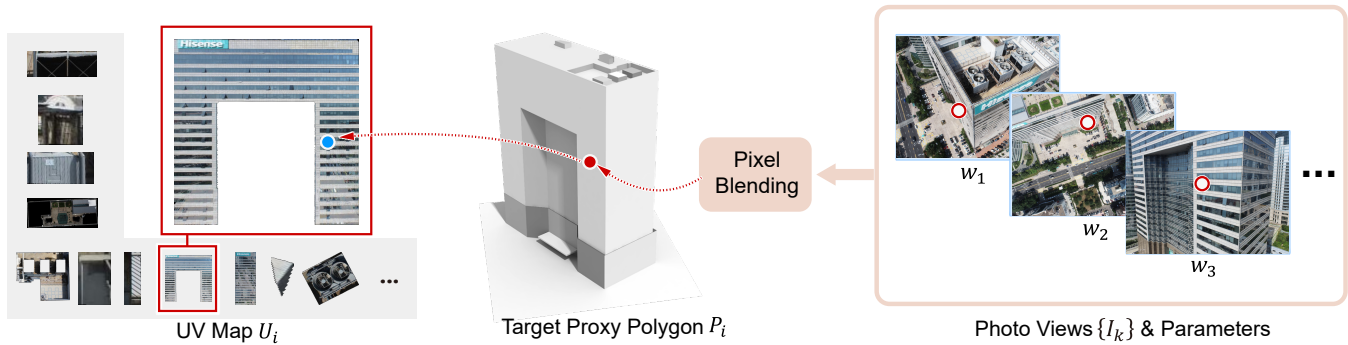


Fig. 1. DiffTex generates realistic texture maps for architectural proxy models. Each texel on the texture map (blue point) is defined as a blend of pixels from photo views (red circles).

Simplified proxy models are commonly used to represent architectural structures, reducing storage requirements and enabling real-time rendering. However, the geometric simplifications inherent in proxies result in a loss of fine color and geometric details, making it essential for textures to compensate for the loss. Preserving the rich texture information from the original dense architectural reconstructions remains a daunting task, particularly when working with unordered RGB photographs. We propose an automated method for generating realistic texture maps for architectural proxy models at the texel level from an unordered collection of registered photographs. Our approach establishes correspondences between texels on a UV map and pixels in the input images, with each texel's color computed as a weighted blend of associated pixel values. Using differentiable rendering, we optimize blending parameters to ensure photometric and perspective consistency,

while maintaining seamless texture coherence. Experimental results demonstrate the effectiveness and robustness of our method across diverse architectural models and varying photographic conditions, enabling the creation of high-quality textures that preserve visual fidelity and structural detail.

CCS Concepts: • **Computing methodologies** → **Shape modeling**.

Additional Key Words and Phrases: Proxy Models, Texture Reconstruction, Differentiable Rendering, Architectural Models

ACM Reference Format:

Weidan Xiong, Yongli Wu, Bochuan Zeng, Jianwei Guo, Dani Lischinski, Daniel Cohen-Or, and Hui Huang. 2025. DiffTex: Differentiable Texturing for Architectural Proxy Models. *ACM Trans. Graph.* 44, 6, Article 184 (December 2025), 13 pages. <https://doi.org/10.1145/3763312>

*Corresponding author: Hui Huang (hhzhiyan@gmail.com)

Authors' addresses: Weidan Xiong, xiongweidan@gmail.com, CSSE, Shenzhen University, China; Yongli Wu, ngligo16@gmail.com, CSSE, Shenzhen University, China; Bochuan Zeng, zbc8301@gmail.com, CSSE, Shenzhen University, China; Jianwei Guo, gjianwei.000@gmail.com, Beijing Normal University, China; Dani Lischinski, danix3d@gmail.com, The Hebrew University of Jerusalem, Israel; Daniel Cohen-Or, cohenor@gmail.com, CSSE, Shenzhen University, China; Hui Huang, hhzhiyan@gmail.com, CSSE, Shenzhen University, China.

Permission to make digital or hard copies of all or part of this work for personal or classroom use is granted without fee provided that copies are not made or distributed for profit or commercial advantage and that copies bear this notice and the full citation on the first page. Copyrights for components of this work owned by others than the author(s) must be honored. Abstracting with credit is permitted. To copy otherwise, or republish, to post on servers or to redistribute to lists, requires prior specific permission and/or a fee. Request permissions from permissions@acm.org.

© 2025 Copyright held by the owner/author(s). Publication rights licensed to ACM. 0730-0301/2025/12-ART184 \$15.00 <https://doi.org/10.1145/3763312>

1 INTRODUCTION

The digital reconstruction of architectural models has long been a central challenge in computer graphics [Garcia-Dorado et al. 2013; Lin et al. 2022; Sinha et al. 2008; Verdie et al. 2015]. Advances in scanning technologies, particularly the proliferation of drone-mounted cameras, have significantly expanded the availability of high-resolution data, enabling the reconstruction of detailed models with remarkable geometric and photometric precision. However, such high-fidelity representations impose substantial computational demands on downstream applications due to challenges in storage, transmission, and real-time rendering.

To alleviate these challenges of dense representations, researchers have explored the generation of these proxies, including procedural modeling, geometric simplification techniques [Gao et al. 2022; Garland and Heckbert 1997; Guo et al. 2024; Salinas et al. 2015], and

manual creation by skilled modelers. These approximations, which trade fine geometric detail for efficiency, dramatically reduce storage and transmission requirements and enable smoother real-time rendering.

Although textures can compensate for the loss of geometric detail, preserving the detailed appearance of the original dense reconstruction is highly challenging following geometric decimation. Specifically, generating realistic texture maps for simplified proxies, from an unordered collection of registered images that were used to reconstruct the original dense model, remains a daunting task.

Existing image-based texture mapping methods [Lempitsky and Ivanov 2007; Sander et al. 2003; Waechter et al. 2014] often struggle when applied to proxy models. These methods frequently introduce distortions in linear features, perspective inconsistencies, and visible seams. Similarly, patch-based optimization methods [Bi et al. 2017; Zhou and Koltun 2014], designed to address photometric issues, often result in blurred textures or incomplete regions, compromising visual quality. Xiong et al. [2023] proposed a method focused on generating texture maps for architectural proxies with enhanced photometric and perspective consistency. However, this approach involves lengthy, intricate procedures and relies heavily on manual fine-tuning to achieve satisfactory results.

In this paper, we propose a novel and versatile approach for texturing architectural proxies using a large set of unordered RGB photographs of a target building. Our method leverages differentiable rendering to generate texel-level UV maps. By utilizing extrinsic camera parameters associated with the input images, we establish precise mappings between UV map texels and image pixels. The RGB value of each texel is computed by blending the corresponding pixel values from the input images, as shown in Fig. 1.

Unlike existing methods that directly optimize RGB values, our approach reconstructs the UV texture by optimizing key intermediate parameters. This results in a reduced search space and enables efficient optimization through differentiable rendering. Our novel texture optimization incorporates loss functions to minimize discrepancies between rendered views and input images, while ensuring the preservation of local features and global structures.

To validate the effectiveness of our method, we conduct extensive experiments on a variety of architecturally diverse buildings. Our results demonstrate the ability of our approach to produce high-quality textured proxies that preserve critical visual features and structural details, ensuring both photometric consistency and visual plausibility.

2 RELATED WORK

3D reconstruction. A typical pipeline for automatic 3D scene reconstruction from a sequence of uncalibrated 2D images consists of two steps: Structure-from-Motion (SfM) [Snavely et al. 2006] first establishes feature correspondences across views and estimates camera poses via incremental or global bundle adjustment, and then the subsequent multi-view stereo (MVS) techniques [Furukawa and Ponce 2009] generate dense point clouds for recovering fine shapes. Although this approach excels in offline and large-scale scene reconstruction, its dependency on static scenes and computational intensity limits its applicability to dynamic or real-time scenarios.

Simultaneous Localization and Mapping (SLAM) addresses this gap by enabling incremental 3D reconstruction while tracking camera pose in real-time, leveraging techniques such as feature-based filtering or direct methods that minimize photometric errors [Engel et al. 2017; Mur-Artal et al. 2015]. In recent years, learning-based approaches [Kerbl et al. 2023; Wang et al. 2025, 2024] have emerged as a powerful paradigm, leveraging deep neural networks to overcome the limitations of traditional methods, introducing end-to-end frameworks that directly regress 3D geometry (such as point clouds, meshes, volumetric representations, neural representations) from images.

Texture mapping for 3D reconstruction. Traditional approaches for mesh texturing are dominated by manual paintings or procedural models [Ebert et al. 2002], and typically require domain-specific expertise and manual efforts. For automatic texture mapping in image-based 3D reconstruction, *view blending* methods [Bernardini et al. 2001; Callieri et al. 2008; Lee et al. 2020] choose multiple visible views for each mesh face (or vertex) and blend these views with different weighted averaging strategies to generate texture patches. Due to geometric and camera calibration errors, textures created by these methods are often blurry and contain ghosting, especially when applied to large-scale objects such as buildings.

In contrast, *selection-based* methods [Fu et al. 2020, 2018; Gal et al. 2010; Lempitsky and Ivanov 2007; Waechter et al. 2014; Wang et al. 2018] assign each face a certain view and extract a texture patch from it, where the selection of optimal view can be formulated as a discrete labeling problem. A Markov random field is constructed to solve this multi-label problem by using different data terms and smoothness terms. Finally, they conduct seam optimization to mitigate visible seams between adjacent patches, yet they remain susceptible to introducing texture-to-texture and texture-to-geometry misalignments.

To further reduce misaligned seams, *warping-based* methods jointly rectify the camera poses and geometric errors. For example, [Zhou and Koltun 2014] and [Bi et al. 2017] use local image warping and patch-based optimization to optimize camera poses while handling large geometry inaccuracies, by correctly aligning the input images. However, these methods are suitable for texturing small objects and carry a high computational cost for large-scale scenes.

To summarize, the above methods can create high-resolution texture maps for dense reconstruction, but the quality of the resultant texture mapping still greatly depends on the quality of geometric reconstruction and the accuracy of camera calibration. None of them can be naively applied to generate realistic texture maps on an abstracted proxy model, because of the significant geometric differences between the proxies and ground-truth dense models.

Texturing proxy geometry. Proxy models can be created manually in CAD software or from procedural modeling [Müller et al. 2006; Schwarz and Müller 2015], or approximated from dense reconstruction by mesh decimation [Gao et al. 2022; Salinas et al. 2015; Verdie et al. 2015] and primitive-based assembly [Bauchet and Lafarge 2020; Bouzas et al. 2020; Fang and Lafarge 2020; Guo et al. 2022; Nan and Wonka 2017]. The abstracted model has significant structural differences from the original dense mesh. However, texturing such

abstracted proxy models has been less explored. A few traditional approaches [Garcia-Dorado et al. 2013; Huang et al. 2017; Maier et al. 2017; Sinha et al. 2008; Wang and Guo 2018] jointly reconstruct abstracted geometry and texture maps by using primitive-based constraints. They still need to select high-quality keyframes from the input image sequence and then perform substantial optimization, so blurring and ghosting artifacts cannot be avoided. Recently, Twin-Tex [Xiong et al. 2023] generated texture maps of architectural proxy considering both perspective and photometric quality. A long sequence of sub-steps is performed to generate a texture map for each proxy polygon, involving fine-tuning a multitude of parameters and requiring long running times.

With the advent of neural fields [Mildenhall et al. 2021; Müller et al. 2022; Xie et al. 2022; Xu et al. 2019], data-driven methods have been proposed to synthesize texture details for low-resolution urban geometry [Georgiou et al. 2021; Kelly et al. 2018], or generate novel-view textures by representing textures in neural networks [Baatz et al. 2022; Metzger et al. 2022; Oechsle et al. 2019; Siddiqui et al. 2022]. Although they can generate various styles of textures, they aim for generation-oriented tasks, *i.e.*, the synthesized textures lack realism compared to the original real scenes. Moreover, high-resolution photorealistic texture maps are hard to generate for Gaussian splatting methods [Huang et al. 2024; Kerbl et al. 2023] due to the high memory requirement, which makes them less applicable in our scenario.

3 OVERVIEW

Given an architectural proxy model represented as a set of planar proxy polygons $\{\mathcal{P}_i\}$, we aim at distilling a high-quality texture map \mathcal{U}_i , for each proxy polygon from a set of unordered, but calibrated (camera parameters are known) RGB photos $\{\mathcal{I}_k\}$.

Each proxy polygon is assigned a 2D UV map. Since \mathcal{P}_i is a planar polygon, rather than using a general mesh parameterization method, we define the UV map by rendering \mathcal{P}_i using a virtual camera perpendicularly facing \mathcal{P}_i , such that the entire polygon fits in its field-of-view. Our goal, then, is to assign the correct color to each UV map texel.

Figures. 1 and 2 show an overview of our method. In the Planar Texture Construction stage (Fig. 2 right), we associate each UV map texel (blue dot) with corresponding pixels in the real images (red circles). In other words, the RGB value of each UV texel t_o is obtained by blending the RGB values of its corresponding image pixels using a set of weights $\{w_i\}$, as shown in Fig. 1. Thus, the texture reconstruction process is formulated as one of optimizing the set of blending weights for each of the texels. In each iteration, these weights, the proxy model and the photo views together are used to reconstruct a texture map for each proxy polygon. Next, the textured proxy is fed into a differential renderer to generate a set of rendered views $\{\mathcal{R}_k\}$ corresponding to the same camera parameters as the real input photos.

We assess the quality of each proxy polygon texture with an objective function L , described below. The gradients of L with respect to the blending weights are then computed via back-propagation, and used to update them. Our objective function L consists of:

- Render loss, L_{Render} , which measures the difference between the rendered views $\{\mathcal{R}_k\}$ and their corresponding photos $\{\mathcal{I}_k\}$. The difference is computed over the selected parts of \mathcal{P}_i in each view.
- Perspective loss, L_{Persp} , which prefers pixels with front-parallel viewing directions, and encourages consistent viewing directions over the entire texture map.
- Parameter loss, L_{Para} , which ensures a smooth parameter field as well as a photometric consistent texture map.

Below, we describe each term of our objective function and the optimization process in more detail.

4 METHOD

Given an unordered collection of N_I photo views $\{\mathcal{I}_k\}$ with arbitrary locations and viewing directions, our goal is to generate a set of realistic texture maps $\{\mathcal{U}_i\}$ for an input proxy with high photometric and perspective consistency.

4.1 Parameters definition

For a UV map \mathcal{U}_i , there is a one-to-one mapping: $f_k^i(\cdot)$ from UV texel coordinates, denoted t_o , to pixel coordinates in image \mathcal{I}_k , denoted p_m . The mapping is given by:

$$p_m = f_k^i(t_o) = K_k \tilde{K}_i^{-1} t_o, \quad (1)$$

where the \tilde{K}_i are the parameters of the virtual camera for the planar parameterization of polygon \mathcal{P}_i and K_k are the parameters of the real camera that captures photo \mathcal{I}_k . The transformations \tilde{K}_i and K_k are fixed after initialization.

The color value $\mathcal{U}_i(t_o)$ of texel t_o can be calculated as the weighted sum of the RGB values of its corresponding pixels $\{\mathcal{I}_k(p_m)\}$ from the input photo collection (N_I images):

$$\mathcal{U}_i(t_o) = \sum_{k=1}^{N_I} w_k \mathcal{I}_k(p_m), \quad (2)$$

where $p_m = f_k^i(t_o)$, and the weights w_k are in $[0, 1]$.

To sum up, we optimize a normalized vector of N_I weights w_k for each texel in \mathcal{U}_i . Thus, each texture map \mathcal{U}_i has a parameter field \mathcal{W}_k^i for \mathcal{I}_k .

4.2 Optimization function

The pipeline of our iterative method is illustrated in Fig. 2. For each proxy polygon \mathcal{P}_i , our method starts with an initial texture map \mathcal{U}_i^0 which is empty. We create a set of binary activation masks $\{a_k^i\}$, each with the same size as \mathcal{I}_k to indicate the selected regions of \mathcal{I}_k in generating \mathcal{U}_i . Initially, a_k^i indicate the regions of \mathcal{P}_i visible in the input photo \mathcal{I}_k .

The weight w_k of \mathcal{I}_k at texel t_o is initialized to $Q(t_o) = Q_a Q_c$. The quality of the viewing angle, Q_a , measures the level of frontality of photo \mathcal{I}_k with respect to \mathcal{P}_i . The quality of color consistency, Q_c , measures the similarity of pixel color $\mathcal{I}_k(p_m)$ to the dominant color among all the corresponding pixels $\{\mathcal{I}_k(p_m)\}$ at t_o . We let $Q_c = \text{Gaussian}(\mathcal{I}_k(p_m), \mu, \sigma)$, where μ and σ is the mean and variance of $\{\mathcal{I}_k(p_m)\}$.

After each iteration, we update $\{a_k^i\}$ by marking the selected pixel (with w_k greater than a very small threshold τ) of \mathcal{I}_k to one, and update to zero if unselected (with $w_k \leq \tau$).

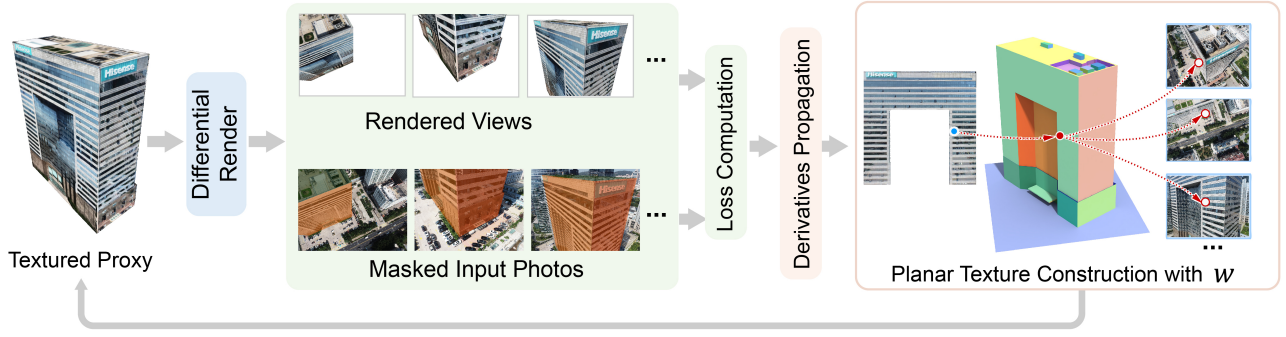


Fig. 2. The differential render renders views to compute a loss, which propagates back to optimize the parameters.

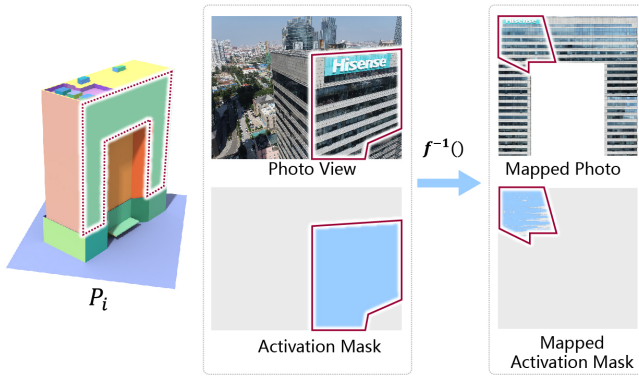


Fig. 3. The photo \mathcal{I}_k^i with binary activation mask a_k^i (left), and the mapped photo $\hat{\mathcal{I}}_k^i$ with mapped \hat{a}_k^i (right) against proxy polygon \mathcal{P}_i of Hisense.

We separately optimize the UV maps of different proxy polygons in parallel. Without loss of generality, we here describe the optimization details of reconstructing the UV map \mathcal{U}_i of proxy polygon \mathcal{P}_i . At iteration t , given the parameters, we first construct each texel in the UV map \mathcal{U}_i^t via the mapping function. Subsequently, all the UV texture maps and the proxy model are employed to generate a textured proxy. The textured proxy is then fed to a differentiable renderer. Next, we measure the quality of the reconstructed texture map \mathcal{U}_i via a loss function as the combination of render loss, perspective loss and parameter loss:

$$L_i = \alpha L_{Render} + \beta L_{Persp} + \omega L_{Para}, \quad (3)$$

where α , β and ω are balancing coefficients for the three loss terms, with default values set to 1, 2, and 10, respectively. At each stage, the parameters are gradually updated to minimize L_i via derivative propagation.

Render Loss. To generate realistic texture maps \mathcal{U}_i for the proxy, we need to minimize the visual discrepancy between the textured proxy and the actual scene. This involves ensuring that the rendered views of the proxy match the input photographs as closely as possible. The rendering loss L_{Render} quantifies the similarity between the rendered views and the actual photos, defined as the sum of pixel-wise squared differences across all selected pixels and a

regularization term:

$$L_{Render} = \sum_k (\|a_k^i \odot Q^i \odot (\mathcal{R}_k - \mathcal{I}_k)\|_2^2 + \sum_o |\mathcal{W}_k^i(t_o)|), \quad (4)$$

where \odot is the element-wise product, Q^i is a quality matrix, matching the size of \mathcal{I}_k , that emphasizes high-quality pixels in the actual photo while eliminating low-quality ones. The regularization term encourages sparsity on the weights of each texel. Each element in Q^i is equal to $Q(t_o)$. The computation of L_{Render} is differentiable, thus making it possible to back-propagate gradients.

Perspective Loss. The photo collections used for building reconstruction often display significant variations in viewing directions, which are vital for camera calibration. However, capturing the same content from different angles can lead to inconsistencies, resulting in ghosting and stretching issues in the reconstructed texture maps. This is particularly problematic for convex/concave facade elements and reflective surfaces such as balconies and windows.

To address this, ideally, the photos used should be taken from a fronto-parallel viewing direction. However, in practice, the input photos often exhibit significant variations in viewing angles, and photos taken from a front direction, or close to it, might not be available. Thus, if we consider the facade normal as a strict constraint, the selected photos may exhibit obvious missing regions.

Therefore, we introduce a guidance viewing direction considering both the consistency of viewing direction and facade normal. The direction vector for the UV map \mathcal{U}_i of facade \mathcal{P}_i is denoted as \tilde{v}_i , which is the average vector of the inverse facade normal and the average viewing direction of visible photos: $\tilde{v}_i = 0.5 * \sum v_k / |\sum v_k| - 0.5 * n_i$, where v_k is the viewing direction of photo \mathcal{I}_k .

We propose a perspective loss, L_{Persp} , to penalize the mapped pixels whose camera directions differ significantly from the guidance viewing direction:

$$L_{Persp} = \sum_k \|\mathcal{W}_k^i \odot \mathcal{V}_k^i \odot \mathcal{V}_k^i\|_1, \quad (5)$$

$$\mathcal{V}_k^i = \hat{a}_k^i \odot (\hat{\mathcal{V}}_k - \tilde{\mathcal{V}}_i). \quad (6)$$

Here, \hat{a}_k^i is the mapped activation mask of a_k^i on \mathcal{P}_i (see Fig. 3), $\hat{\mathcal{V}}_k$ indicates the viewing direction field of photo \mathcal{I}_k , matching the size of \mathcal{U}_i . Each element in $\hat{\mathcal{V}}_k$ corresponds to the inverse viewing

direction of the corresponding pixel in \mathcal{I}_k relative to the camera position. Each element in $\tilde{\mathcal{V}}_i$ is equal to \tilde{v}_i .

Parameter Loss. Optimizing the parameters of neighboring texels independently ignores the coherence of contents and introduces noise. Ensuring that neighboring texels are derived from similar sets of photos can maintain the consistency of content. However, simply insisting that neighboring texels should originate from the same photo can lead to noticeable seams. The Graph-cut algorithm [Kwatra et al. 2003] aims to find a cut in the overlapping region of two images for seamless color transition. We propose a loss, L_{Para} , to encourage parameter smoothness while penalizing neighboring texels exhibiting large color and gradient variations in the overlapping region:

$$L_{Para} = \sum_o \sum_{q \in N(o)} C(t_o, t_q) |\hat{a}_k^i(t_o) \mathcal{W}_k^i(t_o) - \hat{a}_k^i(t_q) \mathcal{W}_k^i(t_q)|, \quad (7)$$

$$C(t_o, t_q) = m_k^i(t_o) D(t_o, t_q) + \lambda_s, \quad (8)$$

$$D(t_o, t_q) = S(\|(\mathcal{U}_i(t_o) - \mathcal{U}_i(t_q))\|_2)(1 + G(t_o)), \quad (9)$$

where $N(o)$ is the up and left neighbors of texel t_o . $\hat{a}_k^i(t_o)$ is the binary value of \hat{a}_k^i at t_o , $\hat{\mathcal{I}}_k^i$ is the mapped \mathcal{I}_k^i on \mathcal{P}_i , m_k^i is the mask denoting the overlap of $\hat{\mathcal{I}}_k^i$ to all the other mapped photos (one for overlap while zero otherwise), $\mathcal{W}_k^i(t_q)$ is the value of \mathcal{W}_k^i at t_q , $S(x)$ is the sigmoid activation function, $G(t_o)$ is the mean of gradient magnitude of all the mapped photos at texel t_o . We set $\lambda_s = 0.5$ in our experiments to balance smoothness and disparity among parameters of neighboring texels. L_{Para} is computed over all mapped images for the texel (summing over k). An element in m_k^i is set to 1 if any other mapped image overlaps with $\hat{\mathcal{I}}_k^i$.

4.3 Data Quality Optimization

Data Elimination. In practice, the input photos often exhibit significant variations in photometric and perspective quality. Simply taking the average of all the corresponding pixels of the target texel introduces severe ghosting and blurring issues. We aim to select only a few semantically coherent photos, thereby letting only a few *key pixels* contribute to the final color value of one texel. To achieve the above goals, we progressively optimize the input data by: i) excluding inclined and perspective inconsistent photos, and \mathcal{I}_k from $\{\mathcal{I}_k\}$ if the portion of zero value weight in \mathcal{W}_k^i (regarding the mask) exceeds a threshold τ_w , ii) eliminating the selected pixel for texel t_o if its color is distinct from the average color of all the selected pixels observing t_o . More specifically, for texel t_o , we compute the mean and standard deviation of its mapped pixel colors, removing any pixels lying outside three standard deviations. We indicate the eliminated pixels in the activation mask as zero.

Improper photo or pixel removal can cause irreversible color loss, as the optimization process cannot infer missing regions. We perform a stress test to validate the effectiveness of our *Data Elimination* by texturing the proxy model given various random subsets of input photos. Please refer to Section D of the supplementary document for more details.

Coarse-to-Fine Resolution. Our texture generation process follows a coarse-to-fine strategy to minimize computational costs while

progressively producing higher-resolution texture maps. Initially, the maximum resolution of the target UV map is set to 256. Typically, neighboring texels share similar parameters. After convergence, we double the texture resolution by upscaling the parameter field using bilinear interpolation. This upscaling process is repeated until the target resolution is reached, i.e., 2048.

Brightness Adjustment. Since each texture map is composed of pixels from various viewing directions, the brightness may be inconsistent across neighboring texels. We perform a histogram matching operation on all the photos to improve the illumination consistency of \mathcal{U}_i in HSV color space.

5 RESULTS

Implementation. Our method is implemented with Nvdiffrast [Laine et al. 2020]. All the presented experimental results are obtained on a desktop computer equipped with an Intel i9-12900k processor with 3.0 GHz, 128 GB RAM and an NVIDIA RTX 3090Ti GPU. We begin with a filtering step that eliminates all the invisible photos, blurry photos, and photos with extremely inclined angles from the inputs. We use the Adam optimizer [Kingma 2014] with default parameters of $\alpha = 0.005$, $\beta_1 = 0.9$, and $\beta_2 = 0.99$, with a constant learning rate throughout training. Additionally, we set $\tau_w = 0.95$ in our experiments.

Dataset. We evaluate the quality of texture maps with synthetic models and real-world buildings (including 14 outdoor buildings, two outdoor scenes and an indoor scene) in this section and supplemental material. We first construct a synthetic dataset containing five virtual models (Hall, Mall, Resident, Archive and Hyundai [Lin et al. 2022]). All the models are created by an in-field modeler. For each model, we rendered 200 views to cover the entire building, all with precise camera parameters without any feature distortions. The real-world scenes come from public sources or are captured by a single-camera drone [Xiong et al. 2023; Zhou et al. 2020]. We use the commercial software RealityCapture¹ (RC) to reconstruct the 3D high-precision models from the captured images. All the abstracted versions are either the 2.5D models for path planning or created by in-field modelers. All of the dense reconstructions and proxy models are utilized to demonstrate the performance of our algorithm. Please refer to the supplementary material for more details and self-evaluation experiments.

5.1 Ablation Study

We utilize a real-world example, called HighRise, to validate the effectiveness of each loss term. The texturing results are visualized in Fig. 4. We can observe that the initialized texture map is blurry and has ghosting issues. One reason is the existence of common errors in the registered camera parameters. The optimized texture map becomes sharper with only L_{Render} , which effectively eliminates photo pixels with large camera errors and photometric disparity. Even so, the results still suffer from blurring issues, as shown in the second column in Fig. 4. Another reason is that, in practice, the captured photos often exhibit biased viewing directions. Most photos are typically taken from a top-down perspective. Large variations in

¹<https://www.capturingreality.com/>

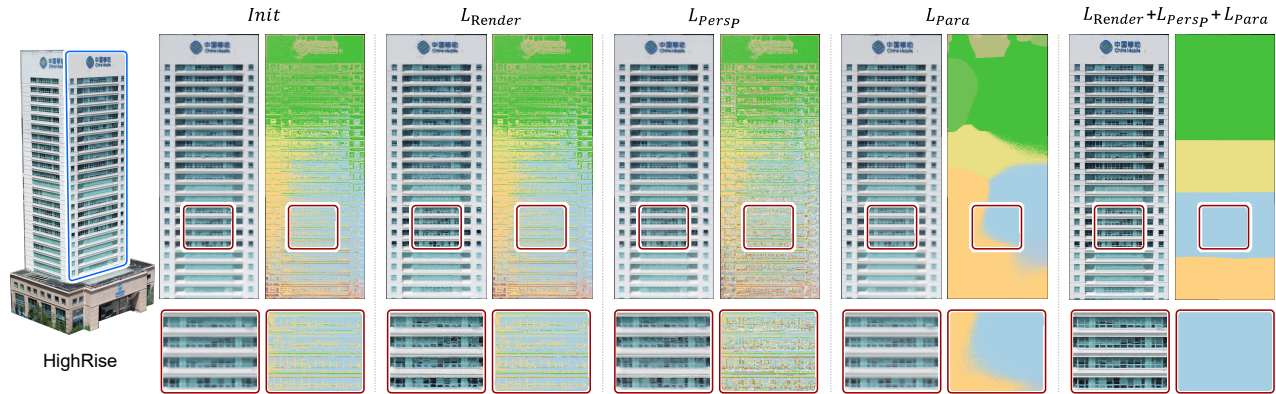


Fig. 4. The initial facade texture maps, and the initial texture maps optimized with L_{Render} , L_{Persp} , L_{Para} , $L_{Render} + L_{Persp} + L_{Para}$ on HighRise example are visualized from left to right. For each facade texture, a texel source map visualizing the photo source (with dominant \mathcal{W} value) of all texels is placed on its right. Each input photo is represented by a unique, randomly assigned color.

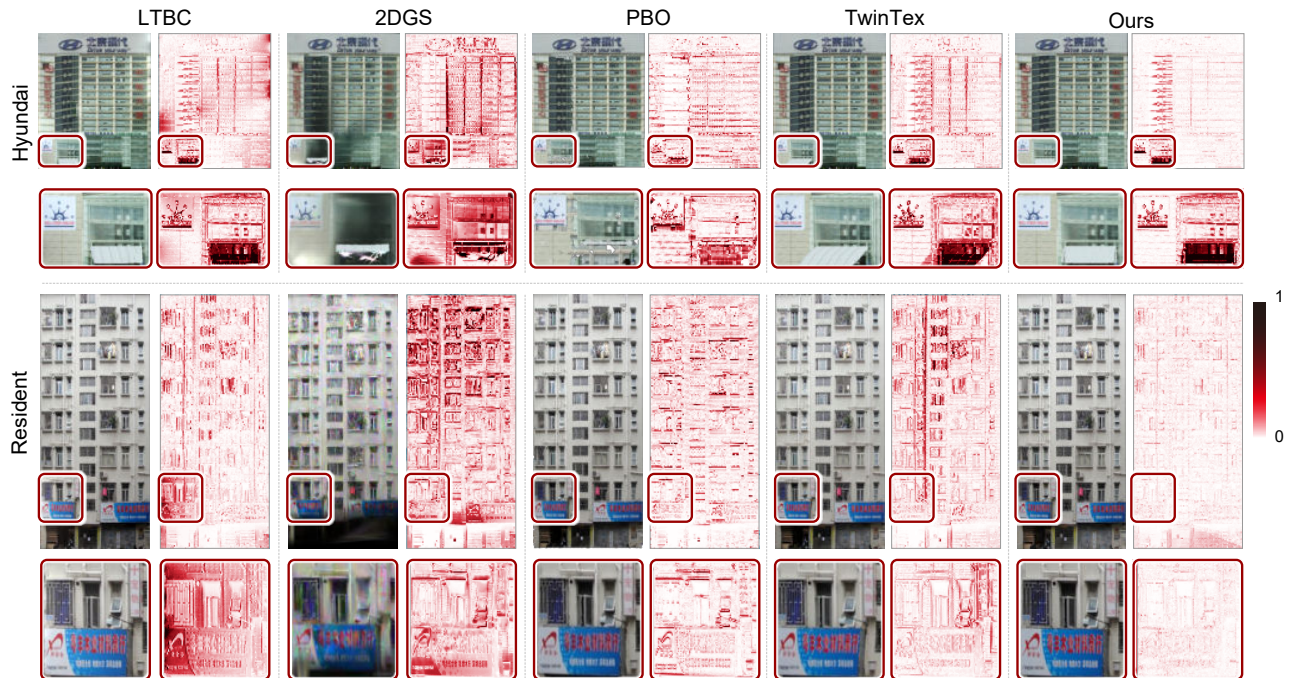


Fig. 5. Comparison with LTBC, 2DGS, PBO, TwinTex and ours on facades of two virtual buildings. The texel-wise differences compared with the GT maps are visualized on the right. The colors denote error values from low (white) to high (dark red).

viewing directions can exist as well. Such variation will bring local blurring issues to regions with convex/concave facade elements. We can alleviate such a problem with only L_{Persp} , e.g., the texture maps on the third column in Fig. 4 reveal higher sharpness. However, the result reveals noisy texels and a lack of content continuity. We then optimize \mathcal{W} with only L_{Para} , encouraging a smooth parameter field. The texture map on the fourth column in Fig. 4 reveals much higher sharpness compared to the first column. However, this still can not address the ghosting issues (see the bottom right region). Our final method, involving all the key components, gives a texture

map with high photometric and high perspective quality. A stress test in the supplementary document (Section D) demonstrates that our method effectively generates high-quality texture maps even under extremely limited resources.

5.2 Comparisons on synthetic Scenes

In this section, we compare our method against multiple methods on both synthetic and real architectural models. Due to the difference in the heuristics among these methods, we perform resampling [Wang et al. 2021] to guarantee their inputs and results share the same

Table 1. Quantitative comparison of the texturing performance on the virtual dataset. Numbers denote the quality values of generated texture maps.

Scene	Method	Error (90%) ↓	Error (95%) ↓	SSIM ↑	LPIPS ↓	Time (min)
Hyundai	LTBC	0.311	0.439	0.831	0.124	0.4
	2DGS	0.449	0.604	0.689	0.323	20.4
	PBO	0.292	0.425	0.761	0.199	32.7
	TwinTex	0.276	0.388	0.779	0.178	1.3
	Ours	0.128	0.277	0.881	0.130	1.2
Resident	LTBC	0.198	0.284	0.807	0.067	0.4
	2DGS	0.588	0.717	0.350	0.535	19.4
	PBO	0.227	0.367	0.675	0.183	13.9
	TwinTex	0.281	0.409	0.669	0.173	10.9
	Ours	0.066	0.092	0.920	0.074	1.2

Table 2. Quantitative comparison on the performance of selected photos and texturing results on real datasets. Numbers in the brackets denote the quality value of the zoomed-in views of each example from top to bottom.

Scene	Method	Perspective Quality		Overall Quality		Time (min)
		Q_{front} ↑	Q_{oc} ↑	SSIM ↑	LPIPS ↓	
Center	RC	-	-	{0.36, 0.40, 0.60, 0.54}	{ 0.49 , 0.43, 0.35, 0.17}	287.0
	LTBC	{0.71, 0.77, 0.71, 0.69}	{0.59, 0.39, 0.59, 0.48}	{0.28, 0.34, 0.27, 0.50}	{0.58, 0.52, 0.32, 0.18}	1.1
	PBO	{0.52, 0.61, 0.52, 0.72}	{0.33, 0.62, 0.33, 0.51}	{0.17, 0.35, 0.62, 0.55}	{0.67, 0.62, 0.36, 0.25}	124.9
	TwinTex	{ 0.89 , 0.98 , 0.89, 0.98 }	{0.78, 0.53, 0.78, 0.77}	{0.12, 0.40, 0.64 , 0.65}	{0.69, 0.49, 0.40, 0.15}	27.2
	Ours	{ 0.91 , 0.93, 0.91 , 0.92}	{ 0.88 , 0.89 , 0.88 , 0.81 }	{ 0.52 , 0.54 , 0.64 , 0.66 }	{0.52, 0.34 , 0.27 , 0.11 }	11.4
Library	RC	-	-	{0.56, 0.65, 0.06, 0.17}	{ 0.44 , 0.39, 0.68, 0.60}	383.6
	LTBC	{0.78, 0.86, 0.67, 0.82}	{0.66, 0.39, 0.25, 0.27}	{0.54, 0.47, 0.14, 0.65}	{0.45, 0.53, 0.27 , 0.37}	1.0
	PBO	{0.94, 0.85, 0.98, 0.89}	{0.93, 0.52, 0.67, 0.27}	{ 0.63 , 0.72, 0.19 , 0.69}	{0.54, 0.46, 0.49, 0.40}	106.4
	TwinTex	{ 0.99 , 0.96 , 0.99 , 0.83}	{0.97, 0.57, 0.71 , 0.80}	{0.59, 0.65, 0.16, 0.70}	{0.46, 0.30, 0.33, 0.39}	35.8
	Ours	{ 0.99 , 0.93, 0.99 , 0.90 }	{ 0.98 , 0.62 , 0.67, 0.90 }	{0.55, 0.73 , 0.18, 0.75 }	{0.47, 0.22 , 0.31, 0.29 }	11.7
Hisense	RC	-	-	{0.52, 0.46, 0.44, 0.45}	{0.32, 0.40, 0.49, 0.42 }	792.3
	LTBC	{0.70, 0.70, 0.51, 0.74}	{0.70, 0.70, 0.38, 0.73}	{0.43, 0.38, 0.35, 0.35}	{0.40, 0.44, 0.51, 0.45}	1.7
	PBO	{0.79, 0.79, 0.67, 0.61}	{0.81, 0.81, 0.38, 0.63}	{0.48, 0.48, 0.46 , 0.46 }	{0.40, 0.36, 0.51, 0.48}	144.6
	TwinTex	{0.86, 0.86, 0.84, 0.54}	{0.85, 0.85, 0.31, 0.54}	{0.56, 0.49 , 0.42, 0.41}	{ 0.31 , 0.34, 0.51, 0.46}	33.7
	Ours	{ 0.92 , 0.92 , 0.93 , 0.96 }	{ 0.92 , 0.92 , 0.90 , 0.96 }	{ 0.57 , 0.48, 0.40, 0.42}	{0.32, 0.33 , 0.48 , 0.46}	14.6
Highrise	RC	-	-	{0.52, 0.31, 0.46, 0.36}	{0.29, 0.45, 0.49, 0.47}	123.0
	LTBC	{0.66, 0.66, 0.79, 0.67}	{0.36, 0.36, 0.56, 0.46}	{0.50, 0.32, 0.50, 0.36}	{0.27, 0.46, 0.43 , 0.46 }	0.8
	PBO	{0.77, 0.77, 0.75, 0.92}	{0.79, 0.79, 0.69, 0.93}	{0.53, 0.48 , 0.53 , 0.40 }	{0.39, 0.43, 0.52, 0.60}	64.7
	TwinTex	{ 0.95 , 0.95 , 0.92 , 0.98}	{0.92, 0.92, 0.66, 0.97}	{0.55, 0.35, 0.52, 0.35}	{0.28, 0.47, 0.45, 0.50}	5.3
	Ours	{ 0.95 , 0.95 , 0.86, 0.99 }	{ 0.94 , 0.94 , 0.70 , 0.98 }	{ 0.58 , 0.45, 0.52, 0.35}	{ 0.25 , 0.34 , 0.47, 0.49}	4.0
PolyTech	RC	-	-	{0.33, 0.22, 0.58, 0.65}	{0.44, 0.19, 0.24, 0.18}	287.0
	LTBC	{0.55, 0.71, 0.48, 0.88}	{0.53, 0.47, 0.33, 0.87 }	{0.34, 0.22, 0.56, 0.68}	{0.39, 0.23, 0.21, 0.31}	4.4
	PBO	{0.68, 0.28, 0.74, 0.94 }	{0.55, 0.32, 0.60, 0.79}	{0.36, 0.22, 0.56, 0.53}	{0.36, 0.48, 0.55, 0.39}	180.3
	TwinTex	{0.54, 0.95 , 0.69, 0.85}	{0.49, 0.56, 0.40, 0.77}	{ 0.42 , 0.25, 0.58, 0.66}	{0.38, 0.33, 0.23, 0.20}	74.2
	Ours	{ 0.90 , 0.92, 0.89 , 0.91}	{ 0.67 , 0.66 , 0.68 , 0.74}	{0.38, 0.26 , 0.65 , 0.70 }	{ 0.28 , 0.18 , 0.16 , 0.15 }	14.1

resolution. Two visual similarity metrics, structural similarity index measure (SSIM) and learned perceptual image patch similarity (LPIPS) [Kasturyulin et al. 2022], are adopted for quantitative evaluation.

Qualitative comparisons. Firstly, we compare our method against let there be color (LTBC) [Waechter et al. 2014], 2D Gaussian Splatting (2DGS) [Huang et al. 2024], patch-based optimization (PBO) [Bi et al. 2017] and TwinTex [Xiong et al. 2023] on synthetic models with precise camera parameters.

For each planar polygon of a virtual model, we regard its UV texture map as the ground truth map. We use the evaluation scheme to compare the texture maps or screenshots to the corresponding ground truth maps. Qualitative results are visualized in Fig. 5. Error maps of resultant maps are provided as well. All the methods achieve feasible results in most cases. However, both LTBC and 2DGS introduced texels with abnormal brightness. All results in Fig. 5 are generated by using the same input set without brightness adjustment. LTBC applies its own adjustment, explaining its

abnormal brightness. Our method and 2DGS do not use such an adjustment. The comparison shows that given the same set of views, 2DGS can generate a scene with satisfying quality in viewing points similar to the input. However, as we move close to the facade at an unseen angle, the results of 2DGS can show cotton-like or needle-like structures. PBO is less stable and sometimes produces empty regions, as shown in the Resident example. Overall, both our method and TwinTex yield plausible results in these cases. However, our approach produces texture maps with significantly fewer errors compared to LTBC, 2DGS, PBO, and TwinTex.

Quantitative comparisons. Quantitative results are listed in Table 1. First, we compute *Error* to assess the quality of the reconstructed texture map by measuring its similarity to the ground truth. Specifically, for each texel, the error is defined as the distance to its corresponding ground-truth color. We then analyze the distribution of these error values and report a threshold x as the error statistic, where x indicates that 95% of texels have a distance smaller than this value. We can see that our Errors are significantly smaller than those of other methods. Moreover, our UV texture maps deliver better SSIM and LPIPS scores [Zhang et al. 2018]. Please refer to the supplementary material for more results. Since our methods and LTBC share different representations of the reconstructed results and tasks compared to 2DGS, the quantitative results may not be fair for either side. Therefore, in subsequent experiments, we only perform comparisons to texturing methods (*i.e.*, excluding 2DGS) that share the same representation to ensure fairness.

5.3 Comparisons on Real Scenes

Qualitative comparisons. For the real scenes, we compare our method against LTBC, patch-based optimization (PBO) [Bi et al. 2017] and TwinTex [Xiong et al. 2023]. We adopt the evaluation scheme in Waechter et al. [2017] and Xiong et al. [2023] to compare the rendered image with the corresponding real image following a specific view from the input cameras. We select the ground truth photos for evaluation from the input excluding the photos for texturing.

Qualitative results are visualized in Fig. 6 and Fig. 7. The dense models reconstructed with RC are shown as references on the facade structure. First, without the constraints on perspective consistency, LTBC failed in selecting photos with both consistent and front-parallel viewing directions, creating obvious seams, perspective inconsistency and “stretching” alike artifacts in the generated textures. The perspective inconsistency can be observed in most of the examples, such as the Center (first and second rows, second column) in Fig. 6, the Highrise example (first row, second column) in Fig. 7. This resulted from merging photos with large viewing angle variance. TwinTex and our method consider both photometric and perspective consistency among selected photos. However, unlike TwinTex, our strategies can select perspective-consistent and front-parallel pixels as much as possible, which yields smoother perspective variation and better frontality in most of the examples. Early-stage decisions that overlook final objectives can create challenges for subsequent steps. TwinTex, for instance, emphasizes minimizing the number of source photos, which may introduce boundary misalignments. In contrast, our method jointly optimizes core goals. For example, to

generate the facade texture in Fig. 4, TwinTex uses only 3 photos, while our approach leverages more, resulting in better perspective alignment and photometric quality across the entire facade. The “stretching” problem can be observed in the inset of the Center (first and third rows, second and fourth columns) building and the Library (six row, second and fourth columns) in Fig. 6, the PolyTech (seven row, fourth column) in Fig. 7, which was caused by using photos with inclined viewing angles. We introduced L_{para} to consider the color distance of source pixels between neighboring texels. This helps generate texels with a higher level of photometric and content consistency compared to TwinTex. The significant improvement can be observed in the Center example in Fig. 6. PBO does not design a photo selection mechanism, is sensitive to the inputs and often generates empty regions. For fair comparisons, we only use a small number of high-quality photos selected by TwinTex and ours as its input. However, PBO still generates results with blurring or ghosting issues.

Quantitative comparisons. Quantitative results on selected photos and texture maps are listed in Table 2.

First, we employ SSIM and LPIPS to evaluate the quality of the final texture maps. Since SSIM is by nature less sensitive to blurring issues and possibly gives higher scores to images with such artifacts [Zhang et al. 2018], the texture with the regional blurring problem could have higher scores. This phenomenon can be observed in some views of the Highrise, Hisense and Library examples. Meanwhile, LPIPS is designed to match human perception and yield better scores for images with a higher level of coherence. In most cases, our UV texture maps can deliver better SSIM and LPIPS scores.

Next, we use the quality metrics in Xiong et al. [2023] to measure the perspective quality of a texture map at the texel level: i) viewing angle frontality Q_{front} , and ii) viewing angle consistency Q_{vc} . All four quality values are normalized to $[0, 1]$. The larger value indicates higher quality. Please refer to the supplemental for more details. Overall, the statistics indicate that our method has the best perspective consistency, while our method and TwinTex achieve the best frontality. This is because the photos are captured by a perspective camera; there are still inclined contents for pixels away from the photo center, even if the photo is taken from a front-parallel angle (especially for large facades). Hence, unlike TwinTex, which selects very few single photos to cover a large plane, we encourage texel-level texture generation, which yields better perspective quality over the entire facade.

Additionally, TwinTex is usually more than two times slower than our method. And PBO’s computational time is often more than three times that of TwinTex, eight times that of our method. Among all the methods, LTBC requires the least running time.

5.4 Challenging Cases

In this subsection, we experiment with more challenging examples and various building styles. Firstly, we experiment on a challenging CSSE example that contains curved surfaces and reflective glass, as shown in Fig. 8. Next, in Fig. 9, we experiment on a temple example with thin pillars and complex structures from public sources [Knapitsch et al. 2017; Zhou et al. 2020]. Finally, we experiment on two complicated scenes with multiple buildings [Zhou et al.

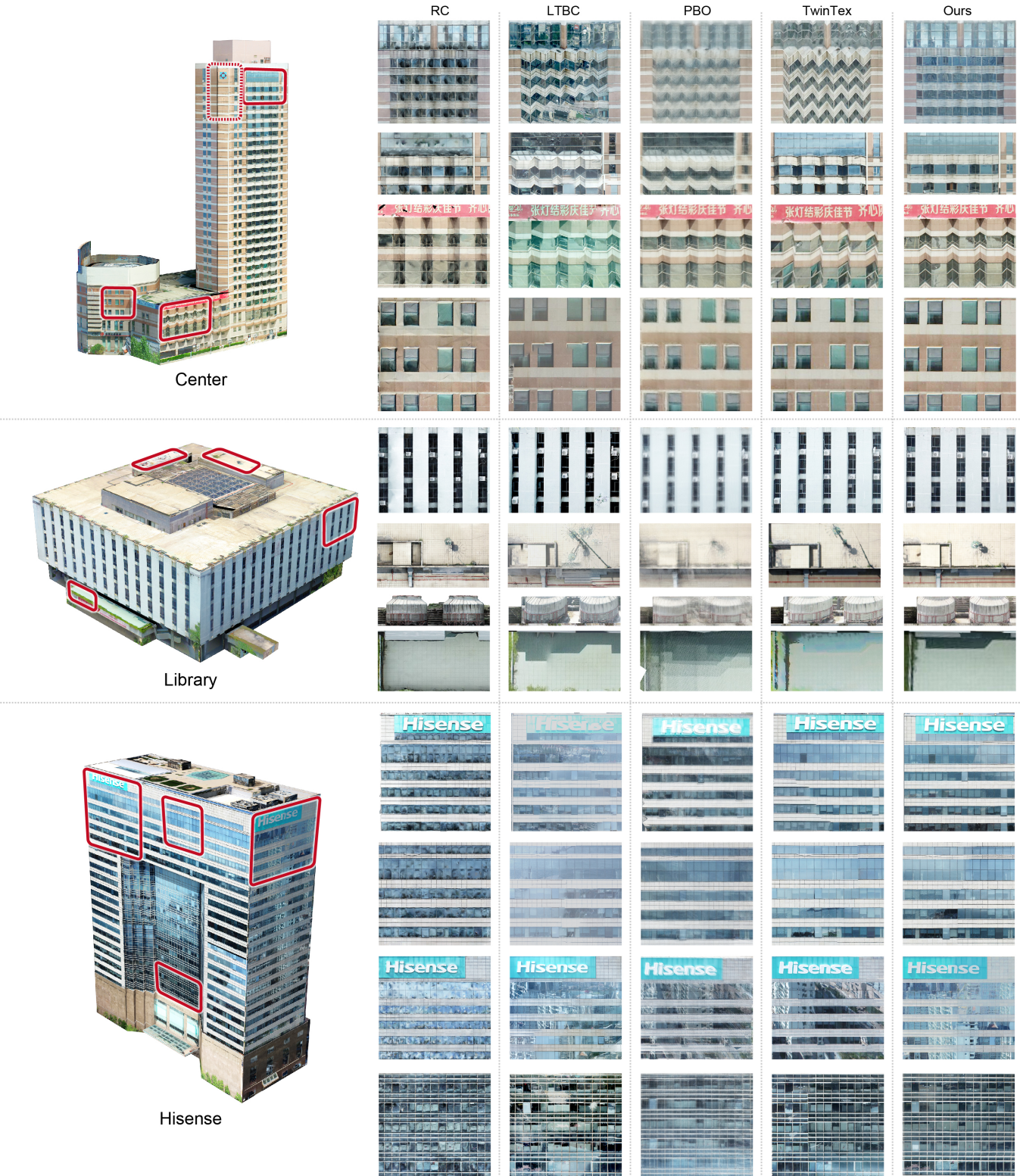


Fig. 6. Comparison of texturing results with RC, LTBC, PBO, TwinTex, and ours on real-world buildings.

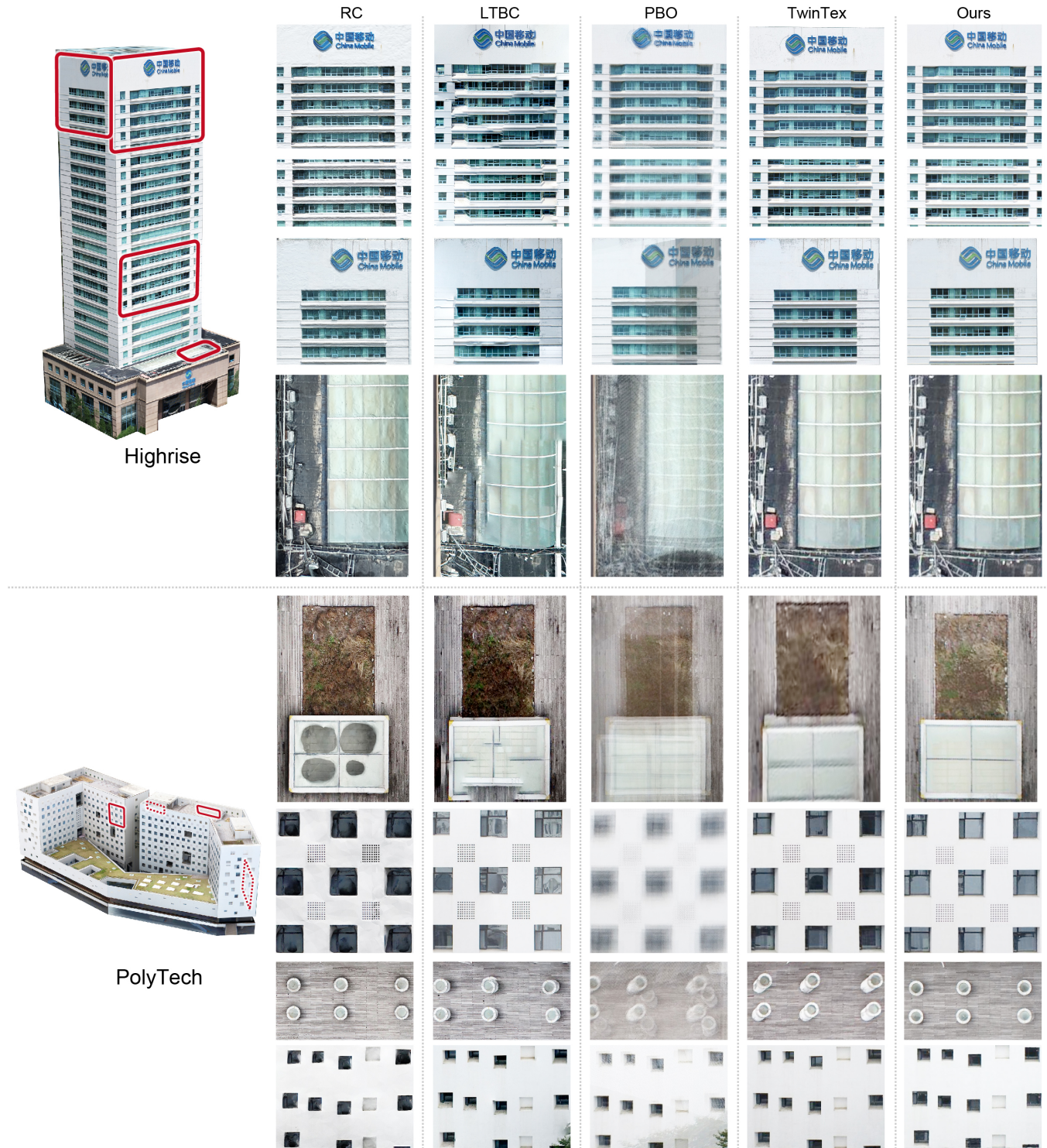


Fig. 7. Comparison of texturing results with RC, LTBC, PBO, TwinTex, and ours on real-world buildings.

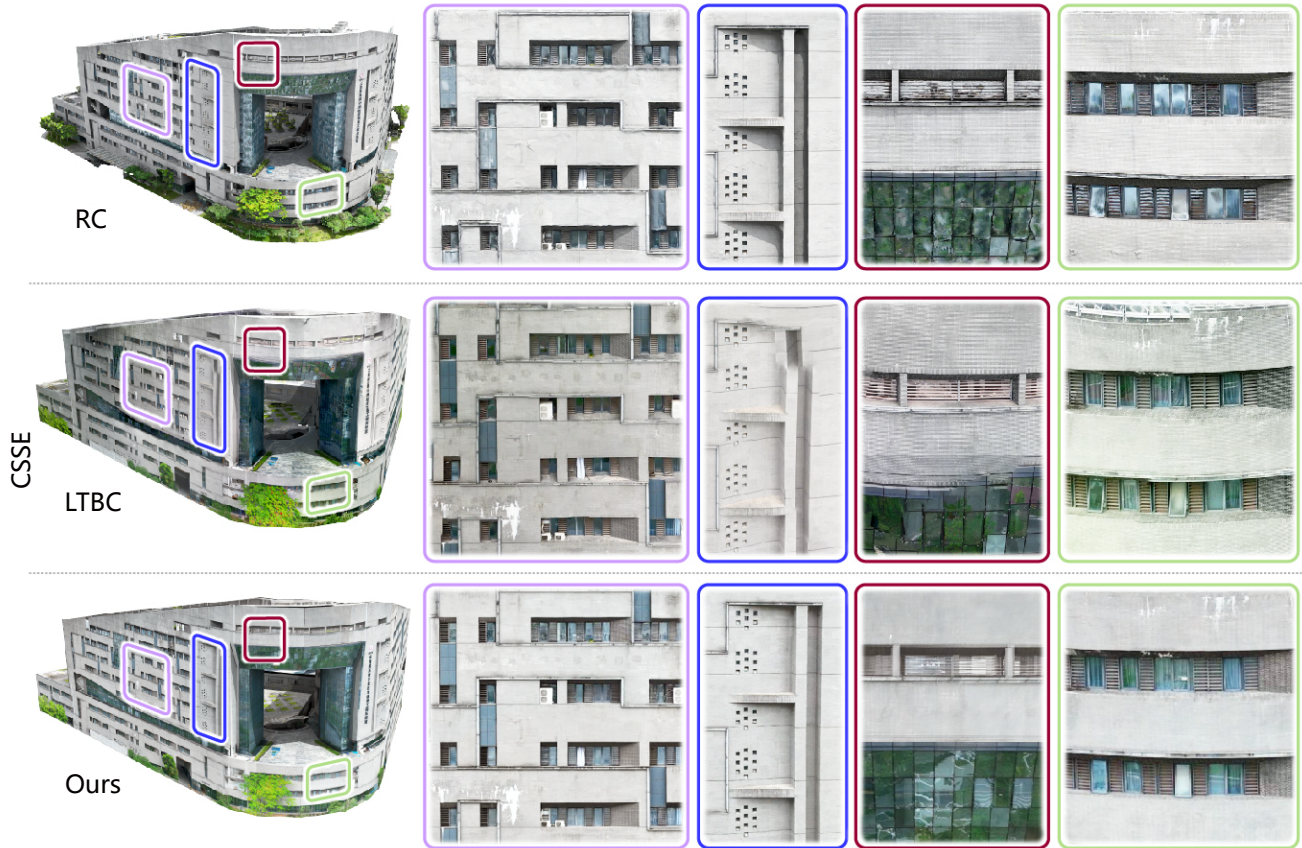


Fig. 8. Comparison of texturing results with RC, LTBC and ours on a challenging CSSE building. The details are shown in the zoomed-in insets.

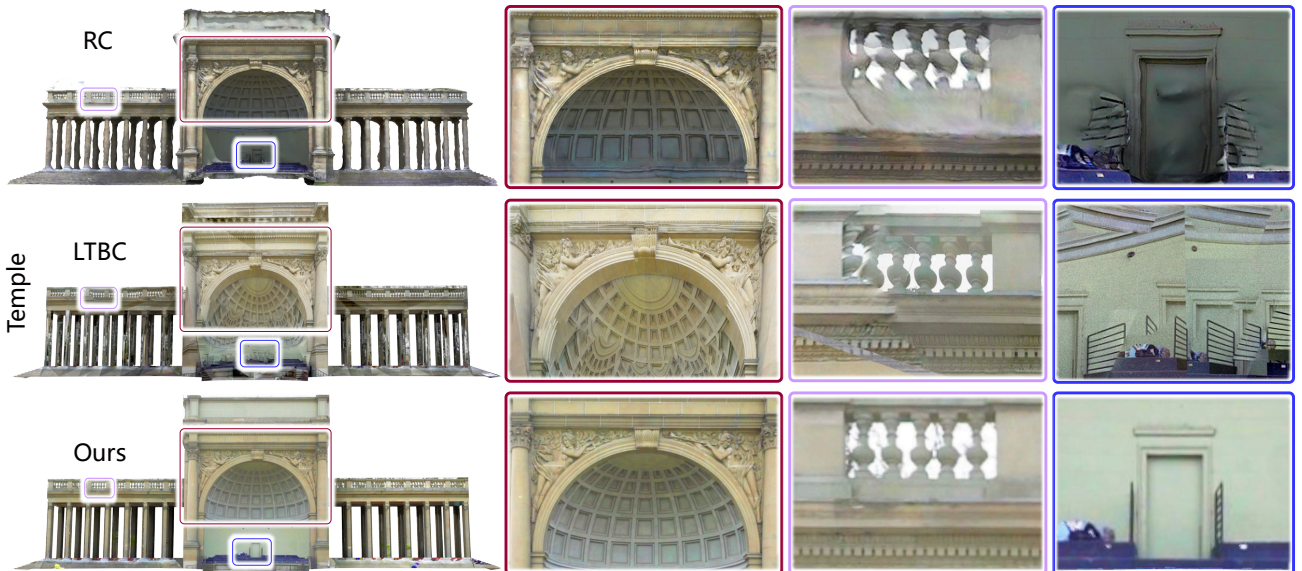


Fig. 9. Comparison of texturing results on the challenging Temple example using RC, LTBC, and our method.

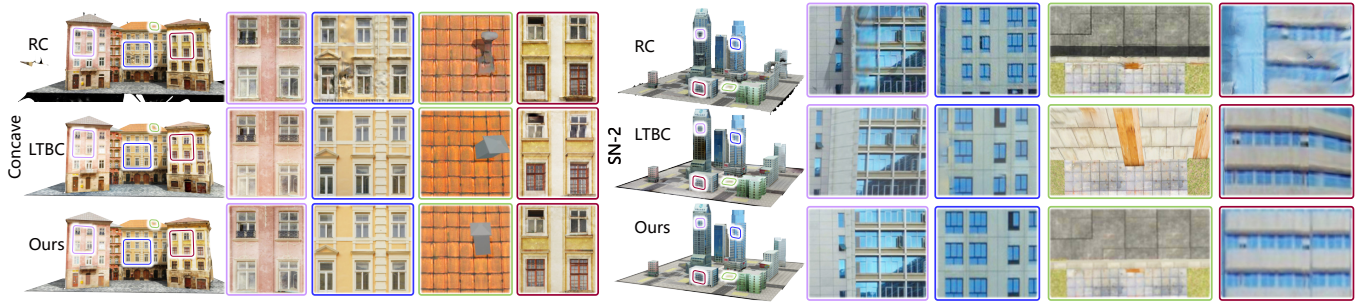


Fig. 10. Comparison of texturing results on two large scenes using RC, LTBC, and our method.



Fig. 11. Failure examples: inter-planar misalignment among two adjacent facades (left), and empty regions covered by none of the input photos (right).

2020], in Fig. 10. The visual results further suggest that the textures generated by our approach exhibit high perspective consistency and harmonious illumination.

6 CONCLUSION AND FUTURE WORK

In this work, we introduce an automated technique for creating realistic texture maps for architectural proxy models using unordered RGB photographs. The core of our approach is to parameterize the texturing process by establishing a correspondence between texels on a UV map and pixels in the input photograph. The color value of each texel is derived as the weighted sum of these associated pixels. We employ differentiable tracing for individual texels to refine blending parameters, ensuring photometric and perspective consistency over a coherent texture map.

Limitations and future work. Our texturing method has several limitations. First, we process each plane independently, which does not consider the mutual relationship among neighboring planes. Fig. 11 (left) shows an example where global alignment of linear features between adjacent planes is not achieved. Note that we here choose a zoomed-in view with the most obvious misalignment among the given buildings to illustrate this issue clearly. Furthermore, since the texturing of each facade polygon is independent, our plans involve expediting this step with parallel processing. Second, for model regions covered by none of the input photos, optimization methods are not able to infer the missing region and create content, see Fig. 11 (right).

Finally, significant occlusion and inaccurate camera parameters may affect the final results. In the future, we would like to introduce a pre-processing step to remove the environmental occlusions.

Another possible future work can be to remove extrinsic camera needs or jointly optimize camera parameters. Furthermore, since we focus on texture optimization, the camera extrinsic parameters are required as input. Possible future works can be removing such needs for extrinsic cameras as in DUST3R [Wang et al. 2024], or jointly optimizing the inaccurate camera parameters.

ACKNOWLEDGMENTS

We thank the reviewers for their constructive comments. This work was supported in parts by Guangdong S&T Program (2024B01015004), NSFC (U21B2023, 62302313, 62572059), ICFCRT (W2441020), Guangdong Basic and Applied Basic Research Foundation (2023B1515120026), Shenzhen Science and Technology Program (KJZD20240903100022028, KQTD20210811090044003, RCJC20200714114435012), and Scientific Development Funds from Shenzhen University.

REFERENCES

- Hendrik Baatz, Jonathan Granskog, Marios Pappas, Fabrice Rousselle, and Jan Novák. 2022. NeRF-Text: Neural Reflectance Field Textures. *Comp. Graph. Forum* 41, 6 (2022), 287–301.
- Jean-Philippe Bauchet and Florent Lafarge. 2020. Kinetic shape reconstruction. *ACM Trans. Graph.* 39, 5 (2020), 156:1–156:14.
- Fausto Bernardini, Ioana M. Martin, and Holly Rushmeier. 2001. High-quality texture reconstruction from multiple scans. *IEEE Trans. on Vis. and Comp. Graph.* 7, 4 (2001), 318–332.
- Sai Bi, Nima Khademi Kalantari, and Ravi Ramamoorthi. 2017. Patch-based optimization for image-based texture mapping. *ACM Trans. Graph. (SIGGRAPH)* 36, 4 (2017), 106:1–106:11.
- Vasileios Bouzas, Hugo Ledoux, and Liangliang Nan. 2020. Structure-aware building mesh polygonization. *ISPRS Journal of Photogrammetry and Remote Sensing* 167 (2020), 432–442.
- Marco Callieri, Paolo Cignoni, Massimiliano Corsini, and Roberto Scopigno. 2008. Masked photo blending: Mapping dense photographic data set on high-resolution sampled 3D models. *Computers & Graphics* 32, 4 (2008), 464–473.
- David S. Ebert, F. Kenton Musgrave, Darwyn Peachey, Ken Perlin, and Steven Worley. 2002. *Texturing and Modeling: A Procedural Approach* (3rd ed.). Morgan Kaufmann Publishers Inc., San Francisco, CA, USA.
- Jakob Engel, Vladlen Koltun, and Daniel Cremers. 2017. Direct sparse odometry. *IEEE Trans. Pattern Anal. Mach. Intell.* 40, 3 (2017), 611–625.
- Hao Fang and Florent Lafarge. 2020. Connect-and-Slice: an hybrid approach for reconstructing 3D objects. In *IEEE Computer Vision and Pattern Recognition (CVPR)*. 13490–13498.
- Yanping Fu, Qingan Yan, Jie Liao, and Chunxia Xiao. 2020. Joint texture and geometry optimization for RGB-D reconstruction. In *IEEE Computer Vision and Pattern Recognition (CVPR)*. 5950–5959.
- Yanping Fu, Qingan Yan, Long Yang, Jie Liao, and Chunxia Xiao. 2018. Texture mapping for 3d reconstruction with RGB-D sensor. In *IEEE Computer Vision and Pattern Recognition (CVPR)*. 4645–4653.
- Yasutaka Furukawa and Jean Ponce. 2009. Accurate, dense, and robust multiview stereopsis. *IEEE Trans. Pattern Anal. Mach. Intell.* 32, 8 (2009), 1362–1376.

- Ran Gal, Yonatan Wexler, Eyal Ofek, Hugues Hoppe, and Daniel Cohen-Or. 2010. Seamless montage for texturing models. *Comp. Graph. Forum* 29, 2 (2010), 479–486.
- Xifeng Gao, Kui Wu, and Zherong Pan. 2022. Low-poly mesh generation for building models. In *ACM SIGGRAPH 2022 Conference Proceedings*. 1–9.
- Ignacio Garcia-Dorado, Ilke Demir, and Daniel G Aliaga. 2013. Automatic urban modeling using volumetric reconstruction with surface graph cuts. *Computers & Graphics* 37, 7 (2013), 896–910.
- Michael Garland and Paul S Heckbert. 1997. Surface simplification using quadric error metrics. In *Proc. ACM SIGGRAPH*. 209–216.
- Yiangos Georgiou, Melinos Averkiou, Tom Kelly, and Evangelos Kalogerakis. 2021. Projective Urban Texturing. In *International Conference on 3D Vision (3DV)*. 1034–1043.
- Jianwei Guo, Yanchao Liu, Xin Song, Haoyu Liu, Xiaopeng Zhang, and Zhanglin Cheng. 2022. Line-Based 3D Building Abstraction and Polygonal Surface Reconstruction From Images. *IEEE Trans. on Vis. and Comp. Graph.* (2022), 1–15.
- Jianwei Guo, Haobo Qin, Yinchang Zhou, Xin Chen, Liangliang Nan, and Hui Huang. 2024. Fast Building Instance Proxy Reconstruction for Large Urban Scenes. *IEEE Trans. Pattern Anal. Mach. Intell.* 46, 11 (2024), 7267–7282.
- Binbin Huang, Zehao Yu, Anpei Chen, Andreas Geiger, and Shenghua Gao. 2024. 2d gaussian splatting for geometrically accurate radiance fields. *arXiv preprint arXiv:2403.17888* (2024).
- Jingwei Huang, Angela Dai, Leonidas J Guibas, and Matthias Nießner. 2017. 3Dlite: towards commodity 3D scanning for content creation. *ACM Trans. Graph. (SIGGRAPH Asia)* 36, 6 (2017), 203:1–203:14.
- Sergey Kastrulyin, Jamil Zakirov, Denis Prokopenko, and Dmitry V Dylov. 2022. PyTorch Image Quality: Metrics for Image Quality Assessment. *arXiv preprint arXiv:2208.14818* (2022).
- Tom Kelly, Paul Guerrero, Anthony Steed, Peter Wonka, and Niloy J. Mitra. 2018. FrankenGAN: Guided Detail Synthesis for Building Mass Models Using Style-Synchronized GANs. *ACM Trans. Graph. (SIGGRAPH Asia)* 37, 6 (2018), 216:1–216:14.
- Bernhard Kerbl, Georgios Kopanas, Thomas Leimkühler, and George Drettakis. 2023. 3D Gaussian Splatting for Real-Time Radiance Field Rendering. *ACM Trans. Graph.* 42, 4 (2023).
- Diederik P Kingma. 2014. Adam: A method for stochastic optimization. *arXiv preprint arXiv:1412.6980* (2014).
- Arno Knapitsch, Jaesik Park, Qian-Yi Zhou, and Vladlen Koltun. 2017. Tanks and temples: Benchmarking large-scale scene reconstruction. *ACM Trans. Graph.* 36, 4 (2017), 1–13.
- Vivek Kwatra, Arno Schödl, Irfan Essa, Greg Turk, and Aaron Bobick. 2003. Graphcut textures: Image and video synthesis using graph cuts. *ACM Trans. Graph.* 22, 3 (2003), 277–286.
- Samuli Laine, Janne Hellsten, Tero Karras, Yeongho Seol, Jaakko Lehtinen, and Timo Aila. 2020. Modular primitives for high-performance differentiable rendering. *ACM Trans. Graph.* 39, 6 (2020), 1–14.
- Joo Ho Lee, Hyunho Ha, Yue Dong, Xin Tong, and Min H Kim. 2020. Texturefusion: High-quality texture acquisition for real-time rgb-d scanning. In *IEEE Computer Vision and Pattern Recognition (CVPR)*. 1272–1280.
- Victor Lempitsky and Denis Ivanov. 2007. Seamless mosaicing of image-based texture maps. In *IEEE Computer Vision and Pattern Recognition (CVPR)*. 1–6.
- Liqiang Lin, Yilin Liu, Yue Hu, Xingguang Yan, Ke Xie, and Hui Huang. 2022. Capturing, Reconstructing, and Simulating: the UrbanScene3D Dataset. In *European Conference on Computer Vision (ECCV)*. 93–109.
- Robert Maier, Kihwan Kim, Daniel Cremers, Jan Kautz, and Matthias Nießner. 2017. Intrinsic3D: High-quality 3D reconstruction by joint appearance and geometry optimization with spatially-varying lighting. In *IEEE International Conference on Computer Vision (ICCV)*. 3114–3122.
- Gal Metzer, Elad Richardson, Or Patashnik, Raja Giryes, and Daniel Cohen-Or. 2022. Latent-NeRF for Shape-Guided Generation of 3D Shapes and Textures. *arXiv preprint arXiv:2211.07600* (2022).
- Ben Mildenhall, Pratul P Srinivasan, Matthew Tancik, Jonathan T Barron, Ravi Ramamoorthi, and Ren Ng. 2021. Nerf: Representing scenes as neural radiance fields for view synthesis. *Commun. ACM* 65, 1 (2021), 99–106.
- Pascal Müller, Peter Wonka, Simon Haegler, Andreas Ulmer, and Luc Van Gool. 2006. Procedural modeling of buildings. *ACM Trans. Graph.* (2006), 614–623.
- Thomas Müller, Alex Evans, Christoph Schied, and Alexander Keller. 2022. Instant Neural Graphics Primitives with a Multiresolution Hash Encoding. *ACM Trans. Graph. (SIGGRAPH)* 41, 4 (2022), 102:1–102:15.
- Raul Mur-Artal, Jose Maria Martinez Montiel, and Juan D Tardos. 2015. ORB-SLAM: A versatile and accurate monocular SLAM system. *IEEE Trans. Robotics* 31, 5 (2015), 1147–1163.
- Liangliang Nan and Peter Wonka. 2017. PolyFit: Polygonal surface reconstruction from point clouds. In *IEEE International Conference on Computer Vision (ICCV)*. 2353–2361.
- Michael Oechsle, Lars Mescheder, Michael Niemeyer, Thilo Strauss, and Andreas Geiger. 2019. Texture fields: Learning texture representations in function space. In *IEEE International Conference on Computer Vision (ICCV)*. 4531–4540.
- David Salinas, Florent Lafarge, and Pierre Alliez. 2015. Structure-aware mesh decimation. *Comp. Graph. Forum* 34, 6 (2015), 211–227.
- Pedro V Sander, Zoë J Wood, Steven Gortler, John Snyder, and Hugues Hoppe. 2003. Multi-chart geometry images. In *Symposium on Geometry Processing*. 146–155.
- Michael Schwarz and Pascal Müller. 2015. Advanced procedural modeling of architecture. *ACM Trans. Graph.* 34, 4 (2015), 1–12.
- Yawar Siddiqui, Justus Thies, Fangchang Ma, Qi Shan, Matthias Nießner, and Angela Dai. 2022. Texturify: Generating textures on 3d shape surfaces. In *European Conference on Computer Vision (ECCV)*. Springer, 72–88.
- Sudipta N Sinha, Drew Steedly, Richard Szeliski, Maneesh Agrawala, and Marc Pollefeys. 2008. Interactive 3D architectural modeling from unordered photo collections. *ACM Trans. Graph.* 27, 5 (2008), 159:1–159:10.
- Noah Snaveley, Steven M Seitz, and Richard Szeliski. 2006. Photo tourism: exploring photo collections in 3D. *ACM Trans. Graph.* 25, 3 (2006), 835–846.
- Yannick Verdie, Florent Lafarge, and Pierre Alliez. 2015. LOD generation for urban scenes. *ACM Trans. Graph.* 34, 3 (2015), 30:1–30:14.
- Michael Waechter, Mate Beljan, Simon Fuhrmann, Nils Moehrl, Johannes Kopf, and Michael Goesele. 2017. Virtual Rephotography: Novel View Prediction Error for 3D Reconstruction. *ACM Trans. Graph.* 36, 1, Article 8 (2017), 11 pages.
- Michael Waechter, Nils Moehrl, and Michael Goesele. 2014. Let there be color! Large-scale texturing of 3D reconstructions. In *European Conference on Computer Vision (ECCV)*. 836–850.
- Bin Wang, Pan Pan, Qinjie Xiao, Likang Luo, Xiaofeng Ren, Rong Jin, and Xiaogang Jin. 2018. Seamless Color Mapping for 3D Reconstruction with Consumer-Grade Scanning Devices. In *European Conference on Computer Vision (ECCV) Workshops*. 633–648.
- Chao Wang and Xiaohu Guo. 2018. Plane-based optimization of geometry and texture for RGB-D reconstruction of indoor scenes. In *International Conference on 3D Vision (3DV)*. 533–541.
- Jianyuan Wang, Minghao Chen, Nikita Karaev, Andrea Vedaldi, Christian Rupprecht, and David Novotny. 2025. Vggt: Visual geometry grounded transformer. In *IEEE Computer Vision and Pattern Recognition (CVPR)*. 5294–5306.
- Shuzhe Wang, Vincent Leroy, Johann Cabon, Boris Chidlovskii, and Jerome Revaud. 2024. DUS3R: Geometric 3D Vision Made Easy. In *IEEE Computer Vision and Pattern Recognition (CVPR)*. 20697–20709.
- Xintao Wang, Liangbin Xie, Chao Dong, and Ying Shan. 2021. Real-esrgan: Training real-world blind super-resolution with pure synthetic data. In *IEEE International Conference on Computer Vision (ICCV)*. 1905–1914.
- Yiheng Xie, Towaki Takikawa, Shunsuke Saito, Or Litany, Shiqin Yan, Numair Khan, Federico Tombari, James Tompkin, Vincent Sitzmann, and Srinath Sridhar. 2022. Neural fields in visual computing and beyond. *Comp. Graph. Forum* 41, 2 (2022), 641–676.
- Weidan Xiong, Hongqian Zhang, Botao Peng, Ziyu Hu, Yongli Wu, Jianwei Guo, and Hui Huang. 2023. TwinTex: Geometry-aware Texture Generation for Abstracted 3D Architectural Models. *ACM Trans. Graph.* 42, 6 (2023), 227:1–227:14.
- Zeixiang Xu, Sai Bi, Kalyan Sunkavalli, Sunil Hadap, Hao Su, and Ravi Ramamoorthi. 2019. Deep view synthesis from sparse photometric images. *ACM Trans. Graph.* 38, 4 (2019), 1–13.
- Richard Zhang, Phillip Isola, Alexei A Efros, Eli Shechtman, and Oliver Wang. 2018. The unreasonable effectiveness of deep features as a perceptual metric. In *IEEE Computer Vision and Pattern Recognition (CVPR)*. 586–595.
- Qian-Yi Zhou and Vladlen Koltun. 2014. Color map optimization for 3D reconstruction with consumer depth cameras. *ACM Trans. Graph. (SIGGRAPH)* 33, 4 (2014), 155:1–155:10.
- Xiaohui Zhou, Ke Xie, Kai Huang, Yilin Liu, Yang Zhou, Minglun Gong, and Hui Huang. 2020. Offsite Aerial Path Planning for Efficient Urban Scene Reconstruction. *ACM Trans. Graph. (SIGGRAPH Asia)* 39, 6 (2020), 192:1–192:16.